Steady shape of a miscible bubble rising below an inclined wall at low Reynolds numbers

Christian Huber*, James M. Watkins, Michael Manga

Department of Earth and Planetary Science, University of California-Berkeley, 307 McCone Hall 4767, Berkeley, CA 94720-4767, USA

A B S T R A C T

When a buoyant volume of fluid impinges a horizontal boundary, it spreads symmetrically in the Stokes flow limit. We investigate the low Reynolds number spreading of a low-viscosity volume of fluid, hereafter called a "bubble", in the limit that the fluids are miscible and interfacial tension can be neglected; the symmetry of the bubble's spreading is broken by allowing the surface to have a finite slope. We use laboratory experiments, parametrized boundary integral numerical calculations, and a scaling argument to show that there exists a steady bubble shape with an aspect ratio (ratio of the semi-axes of the bubble in the horizontal plane) around 1.4–1.6 for slope angles ranging from 5 to 35°. The existence of a steady shape, together with a rapid shift in aspect ratio as the slope angle ϕ increases from 0, suggests a continuous phase transition caused by a loss of symmetry when the finite slope is introduced. We show that the time required for the bubble to reach this steady shape and the constant aspect ratio over the range $10 < \phi < 35$ support the analogy to a phase transition.

© 2008 Elsevier Masson SAS. All rights reserved.

1. Introduction

In an unbounded Newtonian fluid, isolated drops and bubbles (hereafter simply called bubbles) rising at small Reynolds numbers ($\ll 1$), will have a spherical shape [1]. In the absence of interfacial tension, although non-spherical shapes are unstable [2], the shape will evolve to a spherical volume followed by a narrow trailing tail [3–5]. In an unbounded fluid, asymmetry in bubble shapes can be induced by spatially varying interfacial tension [6] or through interactions between bubbles [7,8].

Bubbles will also deform as they approach a boundary. Below a horizontal boundary, bubbles maintain their axisymmetry as they spread (e.g., [9,10]), and symmetry is preserved even if the horizontal interface is deformable [8]. Axisymmetry below a horizontal plane can be broken in two ways; first, below a rigid, no-slip boundary, by gravitational instability in the squeeze film between the bubble and the horizontal surface [11], and second, by viscous fingering due to the Saffman–Taylor instability [12].

Symmetry is also broken if the upper boundary is not horizontal, i.e. its normal is not parallel to gravity. Further, one might expect that as the slope is continuously increased from horizontal to vertical, the asymmetry of the bubble in the two dimensions parallel to the slope will increase continuously with the projection of the buoyancy force along the inclined boundary.

The shape of gravity currents on a sloping surface has been studied for the case in which (1) the fluids are miscible and the spreading fluid is more viscous than the surroundings [13,14] and (2) the fluids are immiscible and the spreading fluid is less viscous than the surroundings [15–17]. Here, in contrast, we focus on the limit in which the spreading bubble is much less viscous than the ambient fluid and the two fluids are miscible, so that interfacial tension plays no dynamic role. This problem is motivated by geophysical applications in which mantle plumes rise towards the Earth's surface and encounter a sloping boundary. This occurs next to mid-ocean ridges [18,19] and if plumes encounter a subducting plate [20,21].

Accordingly, in this paper we consider the shape and motion of a miscible bubble moving at low Reynolds number below a rigid, sloping, no-slip boundary. We first describe laboratory experiments that reveal (1) the existence of a steady configuration for bubbles below finite boundary slopes and (2) a relationship between the slope and the bubble aspect ratio that was unexpected. Next, in order to understand some of the experimental observations, we use a numerical boundary integral method and idealization of the bubble shape to find solutions for the aspect ratio and speed of the bubbles. Finally, we present some scaling arguments to explain the main features of the bubbles.

2. Experiments

Our experiments are designed to monitor the shape and velocity of a positively buoyant bubble as it rises, impinges and deforms beneath an inclined boundary. We use two miscible Newtonian flu-
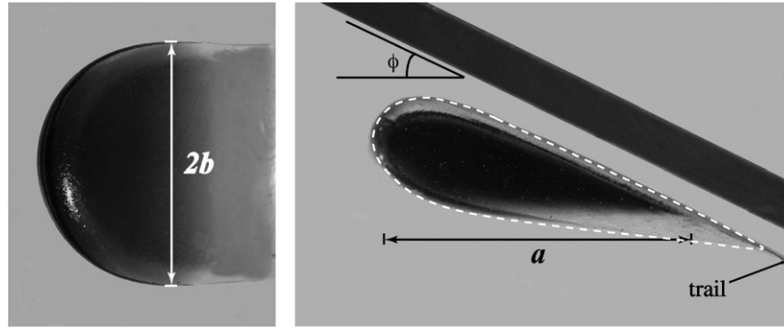
Fig. 1. Top and side views of a bubble with a steady shape (flat bottom, front bulge) for $\phi = 20°$. The bubble width $2b$ is measured from the top view and the bubble length a is measured from the side view, as shown. The trail behind the bubble represents volume loss by diffusion, which is important only at small angles ($\phi \lesssim 5°$). The halo surrounding the bubble, highlighted by the white dashed line, is an optical effect due to the bubble's curvature.

Table 1
Summary of experiments.

ϕ (°)	V (cm³)	μ (Pa s)	λ	Aspect ratio r	u_x/U	t^*	d^*
3.0	25.0 ± 0.1	462 ± 12	(2.16 ± 0.01)10⁻⁵	1.85 ± 0.13	0.004 ± 0.002	330 ± 70	4 ± 0.55
5.0	30.52 ± 0.1	447 ± 12	(2.24 ± 0.01)10⁻⁵	1.50 ± 0.11	0.016 ± 0.002	343 ± 70	7 ± 1.3
10	40.75 ± 0.1	594 ± 13	(1.69 ± 0.01)10⁻⁵	1.40 ± 0.05	0.039 ± 0.003	99 ± 9.6	5 ± 0.5
13.5	14.0 ± 0.1	393 ± 12	(2.55 ± 0.01)10⁻⁵	1.43 ± 0.04	0.048 ± 0.004	112 ± 9.3	7.6 ± 0.9
18.0	19.0 ± 0.1	361 ± 11	(2.78 ± 0.01)10⁻⁵	1.43 ± 0.04	0.070 ± 0.003	72 ± 6	5.7 ± 0.4
19.5	16.5 ± 0.1	393 ± 12	(2.55 ± 0.01)10⁻⁵	1.38 ± 0.03	0.091 ± 0.005	53 ± 5.3	5.8 ± 0.5
20.5	6.9 ± 0.1	347 ± 11	(2.88 ± 0.01)10⁻⁵	1.58 ± 0.04	0.085 ± 0.006	54 ± 4.5	4.8 ± 0.3
24.0	18.5 ± 0.1	370 ± 11	(2.71 ± 0.01)10⁻⁵	1.44 ± 0.10	0.099 ± 0.005	47 ± 5.9	5 ± 0.6
27.0	14.9 ± 0.1	396 ± 12	(2.53 ± 0.01)10⁻⁵	1.45 ± 0.03	0.112 ± 0.006	45 ± 5.1	3.8 ± 0.7
31.5	16.5 ± 0.1	384 ± 12	(2.61 ± 0.01)10⁻⁵	1.48 ± 0.04	0.135 ± 0.006	49 ± 5.4	3.4 ± 0.7
35.5	18.2 ± 0.1	393 ± 12	(2.55 ± 0.01)10⁻⁵	1.58 ± 0.03	0.135 ± 0.006	55 ± 5.5	4.5 ± 0.7
36.0	14.8 ± 0.1	396 ± 12	(2.53 ± 0.01)10⁻⁵	1.50 ± 0.13	0.140 ± 0.006	51 ± 10	7.2 ± 1

ids (corn syrup and water) so that interfacial tension effects can be neglected. Our previous experiments with similar fluids show no features that can be attributed to interfacial tension, at least at length scales and time scales we consider [22]. To begin each experiment, a buoyant bubble (radius ≈ 1.5 cm) is made by injecting water into a tank filled with corn syrup. The upper boundary is a rigid plexiglass plate set at fixed angle within the syrup. The top and side views of the bubble are recorded on video cameras that are synchronized by a timer.

In these experiments, we control bubble volume and the angle of the upper boundary. The density of water and corn syrup are measured using an Anton Paar density meter capable of µg/cm³ precision. The density difference between the bubble and the ambiant fluid is $|\Delta\rho| = 0.4474$ g/cm³. The largest source of uncertainty is the corn syrup viscosity μ_1, which is sensitive to temperature fluctuations in the laboratory (dμ_1/d$T \approx 50$ Pa s/°C and $\mu_1 \approx 350$ Pa s at 25 °C, where T is temperature). Because syrup viscosity is not controlled, it is determined before and after each experiment by measuring the speed at which a steel sphere (radius = 0.0032 m, density = 7.974 g/cm⁻³) descends in the corn syrup. Comparison of repeated measurements in each experiment supports our estimated precision for syrup viscosity of ±12 Pa s.

We use a large tank (60 × 30 × 30 cm) compared to the size of bubble to minimize the effect of the sides of the tank. The duration of most experiments is short (about 10 minutes) compared to the timescale of diffusion between the fluids, so we neglect any diffusive mass loss from the bubble. The diffusion length-scale is about 0.6 mm for the duration of the experiments, using the diffusivities from [23]. After each experiment, most of the water is removed from the tank, though some persists as a thin layer along the bubble's ascent path (see Fig. 1). To avoid the effect of a low-viscosity conduit from previous runs [24], we stir the syrup and allow it to homogenize for at least two days between experiments.

We measure the length a of the bubble from the side view (Fig. 1(right)) and the width b from the top view (Fig. 1(left)).

We observe that the bubble reaches a steady shape (constant ratio $r = a/b$ with flat bottom; see Fig. 1) that is maintained as it rises along the upper boundary at constant velocity. We measure the steady shape (aspect ratio) and velocity as a function of boundary inclination using millimeter-scale grids attached to the upper boundary and sides of the tank. Results from the experiments are summarized in Table 1.

3. Theoretical model

In order to better understand the parameters that govern the bubble shape and velocity, we now develop a theoretical model for a geometrically simplified shape. As the system we consider is controlled by buoyancy and viscous forces, the dynamics of the two fluids are described by Stokes equations

$$\begin{cases} \nabla \cdot \mathbf{T}_1 = -\nabla p + \mu_1 \nabla^2 \mathbf{u}_1 + \rho_1 \mathbf{g} = \mathbf{0}, \\ \nabla \cdot \mathbf{u}_1 = 0, \end{cases} \tag{1}$$

$$\begin{cases} \nabla \cdot \mathbf{T}_2 = -\nabla p + \mu_2 \nabla^2 \mathbf{u}_2 + \rho_2 \mathbf{g} = \mathbf{0}, \\ \nabla \cdot \mathbf{u}_2 = 0 \end{cases} \tag{2}$$

where $\mathbf{T}_i$ is the stress tensor, $\mathbf{g}$ is the acceleration due to gravity, p is the pressure, $\mathbf{u}_i$ and μ_i are the velocity and the dynamic viscosity of fluid i, respectively.

We make the equations dimensionless by introducing the length-scale $R = \sqrt[3]{3V/4\pi}$ and the velocity $U = \Delta\rho g R^2/\mu_1$, where V is the volume of the bubble and $\Delta\rho = \rho_1 - \rho_2$. We also introduce the dimensionless viscosity ratio $\lambda = \mu_2/\mu_1$, that we fix to 2.5×10^{-5} for each calculation.

Using an integral representation of Stokes flow allows us to describe the velocity at the interface as a function of the interface stress drop and the velocity distribution as

$$\frac{1}{2}\mathbf{u}(\mathbf{x}_0) = -\frac{1}{8\pi}\frac{1}{\lambda + 1}\int_S \langle \hat{\mathbf{n}} \cdot \mathbf{T} \rangle \cdot \mathbf{J}\,dS + \frac{1}{8\pi}\frac{1 - \lambda}{1 + \lambda}\int_S \mathbf{u} \cdot \mathbf{K} \cdot \hat{\mathbf{n}}\,dS \tag{3}$$

where $\mathbf{x}_0$ is a point located on the interface between the fluids S, $\hat{\mathbf{n}}$ is the normal to the surface S (pointing out of fluid 2), $\langle \hat{\mathbf{n}} \cdot \mathbf{T} \rangle$ is the stress jump across the interface (includes the buoyancy term), and $\|\mathbf{x} - \mathbf{x}_0\|$ is the distance between the observation and the integration points. Eq. (3) is a principal value integral as $\mathbf{x}_0$ is by definition located on the surface over which the integration is calculated. The velocity kernel $\mathbf{J}$ and its associated stress tensor $\mathbf{K}$ describe the velocity and stress from a point force, respectively.

In the case where we neglect surface tension, the stress jump reduces to

$$\langle \hat{\mathbf{n}} \cdot \mathbf{T} \rangle = (\hat{\mathbf{g}} \cdot \hat{\mathbf{x}}) \hat{\mathbf{n}} \tag{4}$$

where $\hat{\mathbf{g}}$ refers to a unit vector in the direction of $\mathbf{g}$ and $\hat{\mathbf{x}} = \mathbf{x}/R$. The model can be extended to immiscible fluids by introducing surface tension in the stress term.

The no-slip boundary condition is introduced using the Lorentz–Blake Green's function for a semi-infinite flow bounded by a plane wall ([25,26], see Appendix A for a more detailed description):

$$\mathbf{J}(\mathbf{x}_0, \mathbf{x}) = \mathbf{J}^{St}(\hat{\mathbf{x}}) - \mathbf{J}^{St}(\hat{\mathbf{X}}) + 2h^2 \mathbf{J}^D(\hat{\mathbf{X}}) - 2h \mathbf{J}^{SD}(\hat{\mathbf{X}}) \tag{5}$$

where $\mathbf{J}^{St}$ is the Stokeslet, h is the distance between the integration point and the wall, $\hat{\mathbf{x}} = \mathbf{x}_0 - \mathbf{x}$ and $\hat{\mathbf{X}} = \mathbf{x}_0 - \mathbf{x}^{IM}$ is the vector connecting the observation point and the image of the integration point. $\mathbf{J}^D(\hat{\mathbf{X}})$ is the dipole term and $\mathbf{J}^{SD}(\hat{\mathbf{X}})$ is the doublet. Similarly, we can define the Green's function for the stress:

$$\mathbf{K}(\mathbf{x}, \mathbf{x}_0) = \mathbf{K}(\hat{\mathbf{x}}) - \mathbf{K}(\hat{\mathbf{X}}) + 2h_0^2 \mathbf{K}^D(\hat{\mathbf{X}}) - 2h_0 \mathbf{K}^{SD}(\hat{\mathbf{X}}) \tag{6}$$

where h_0 is the distance between the observation point and the wall, $\hat{\mathbf{x}} = \mathbf{x} - \mathbf{x}_0$ and $\hat{\mathbf{X}} = \mathbf{x} - \mathbf{x}_0^{IM}$. The overall stress tensor is a combination of the Stresslet, the Stresslet at the image point, a dipole term and the doublet.

The image method has been used extensively for problems with boundaries [10,25–27] and permits inclusion of the no-slip condition at the wall explicitly. Among all these terms, only the Stokeslet and Stresslet are singular as the singularities at the wall interface are canceled by $h_0 = 0$ in the other terms.

We can estimate the time to reach the steady-state shape using the velocity distribution obtained from Eq. (3). Using the differential x velocity component between the bubble's front ($u_x(\theta = 0)$) and the center of mass (u_x^{CM}), we can monitor readjustments of the bubble shape as it approaches the steady-state. We compute the time it takes for the bubble to reach 95% of its deformation from an axisymmetric ($r = a/b = 2$) shape to the steady aspect ratio (r_g)

$$t(\phi) = - \int_2^{r^*} \frac{\delta a(r)}{u_x(\theta = 0, r, \phi) - u_x^{CM}} \, dr \tag{7}$$

where $r^* = 2 - 0.95(2 - r_g)$ and $\delta a(r)$ represents the length change of the bubble for a change in aspect ratio dr. V is the bubble volume, θ is the angle describing the azimuthal position on the parametrized surface, and ϕ is again the angle between the upper boundary and a horizontal plane (see Fig. 2).

4. Numerical implementation

We solve for the aspect ratio of the bubble at steady-state by first defining a family of bubble shapes with a single free parameter: the aspect ratio r (see Fig. 2). The choice of a single free parameter and the generic shape stems from laboratory observations. The aim is also to find the simplest model that captures the physics observed in the experiments. Among this family of shapes, we define the "best shape" as the shape which best satisfies the kinematic boundary condition on the surface of a bubble with a steady shape. In order to solve Eq. (3) we need to parameterize
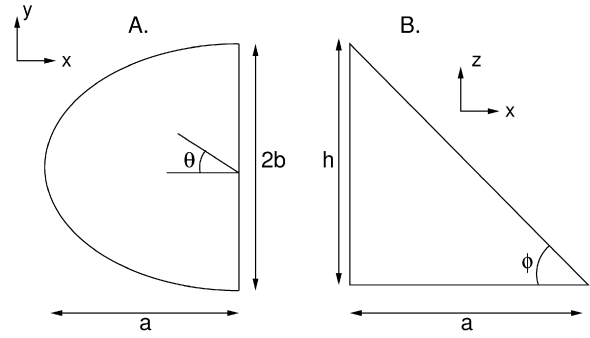
Fig. 2. Parameterization used for the numerical model. A. View from above (along z-axis). B. Side view (along y-axis).

the interface. Using observations from experiments, we define our parameterization Φ (see Fig. 2) by

$$\Phi : \mathbb{R}^2 \longrightarrow \mathbb{R}^3,$$
$$(\theta, z) \overset{\Phi}{\mapsto} (a - a\cos\theta, -b\sin\theta, z) \tag{8}$$

where $-\frac{\pi}{2} \leqslant \theta \leqslant \frac{\pi}{2}$ and $0 \leqslant z \leqslant a\tan\phi\cos\theta$. The lower ($z = 0$) surface and its image do not contribute to the integrals because they are free-slip boundaries and isobaric surfaces. The surface along the wall ($z = a\tan\phi\cos\theta$) is canceled from the integrals in Eq. (3) by the choice of Green's functions. In the absence of capillary effects and in the limit $\lambda \ll 1$, we neglect the effect of the squeeze layer between the bubble and the wall [17,28]. We justify this approximation by arguing that a narrow film (thickness δ) of high viscosity fluid in contact with a wall can be approximated by a no-slip boundary. As the stresses responsible for the motion of the bubble scale with its buoyancy, and since corn syrup viscosity is several orders of magnitude higher than that of water, the velocity gradients in the squeeze layer are small. In addition, because of the small relative size of the squeeze layer δ compared to a or b, we can assume a no-slip boundary condition between the bubble and fluid in the squeeze layer.

Because the stress jump is known for our parametrization, Eq. (3) is a Fredholm integral equation of the second kind. The two integrals of Eq. (3) contain a singularity at $\mathbf{x} = \mathbf{x}_0$. In the first integral, the singularity can be removed analytically by applying a singularity subtraction. The singularity in the second integral is treated by meshing the surface into low-curvature stripes to cancel the contribution of the product $\mathbf{x} \cdot \hat{\mathbf{n}}$ (from the product $\mathbf{K} \cdot \hat{\mathbf{n}}$) in the stripe containing the singularity.

In order to solve the surface integrals in Eq. (3), we begin by meshing the surface into N stripes (according to θ) delimited by

$$-\frac{\pi}{2} + m\frac{\pi}{N} \leqslant \theta_m \leqslant -\frac{\pi}{2} + (m+1)\frac{\pi}{N}, \quad m = 0, \dots, N-1,$$
$$0 \leqslant z_m \leqslant \tan\phi\cos(\theta_m). \tag{9}$$

We then assume constant velocity on each element and construct a linear system from Eq. (3). The surface integrals over each stripe are calculated by an eight point Gauss–Legendre quadrature scheme in each of the two dimensions (z, θ). The steady-shape should satisfy the kinematic condition

$$(\mathbf{u} - \langle \mathbf{u} \rangle) \cdot \hat{\mathbf{n}} = 0 \tag{10}$$

at every point on the surface of the bubble, $\langle \mathbf{u} \rangle$ is the velocity of the bubble's center of mass. We then define the dimensionless parameter

$$D\left(r = \frac{a}{b}\right) = \frac{1}{A|\langle u \rangle|} \int_S \left| (\mathbf{u} - \langle \mathbf{u} \rangle) \cdot \hat{\mathbf{n}} \right| dS \tag{11}$$
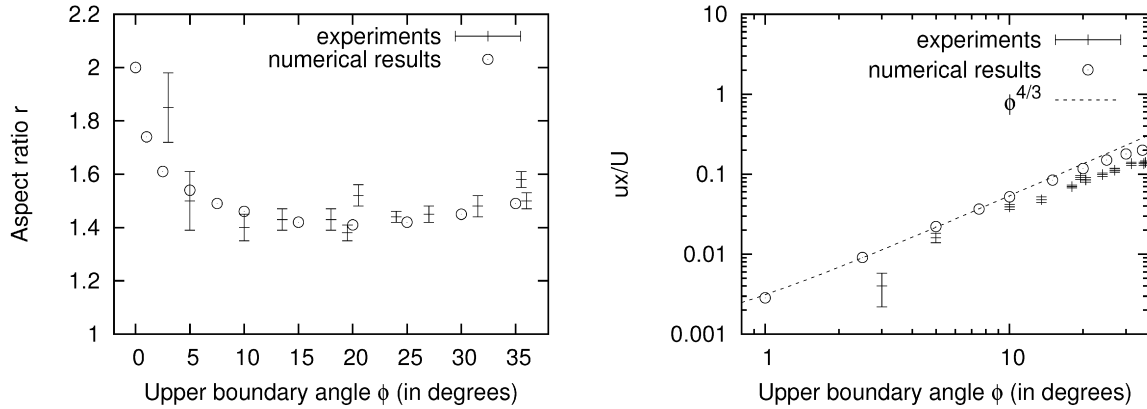
Fig. 3. (left) Comparison of the steady aspect ratio ($r = a/b$) obtained from the laboratory experiments with parametrized numerical calculations. See text for discussion. (right) Comparison of the bubble velocity in the *x*-direction between experiments and numerical calculation. The scaling relation obtained in Eq. (17) is shown for reference. The error bars for the numerical calculations are smaller than the symbols.

where A is the area of the surface we parameterize and $|\langle u \rangle|$ is estimated from the magnitude of the x component of velocity at the front of the bubble ($\theta = 0$). D is a measure of the deviation from the steady-state velocity for a given choice of aspect ratio. As we adopt a simplified parameterization of the bubble geometry that describes the general shape of the bubbles in our experiments, D will not be zero but has a minimum value (> 0 for this idealized case) for the aspect ratio that best approximates the steady shape.

For a numerical solution, Eq. (7) can be discretized to

$$t = \sum_{k=2}^{N_{\text{steps}}} \frac{\sqrt[3]{3Vr_{k-1}/(2\tan\phi)} - \sqrt[3]{3Vr_k/(2\tan\phi)}}{|u_x(\theta = 0, k-1) - u_x^{CM}(r_g)|}. \quad (12)$$

The sum is calculated from $r = 2$ (corresponding to $k = 1$) to $r^* = 2 - 0.95(2 - r_g)$ (corresponding to $k = N_{\text{steps}}$). The numerator represents the length change in the x direction associated with the readjustment of the bubble shape.

5. Results and discussion

For a bubble spreading beneath a horizontal boundary, the aspect ratio a/b is 2 because of the symmetry of the problem. The bubble will spread indefinitely if we neglect molecular scale effects yet maintain an axisymmetric shape (e.g. [11,29]).

For the case with a sloping upper boundary, our numerical results reveal the existence of a single minimum of D. In addition, the velocity distribution shows that the bubble shape adjusts to converge to the aspect ratio which corresponds to the minimum of D. These two observations point to the existence of a steady shape, consistent with our experimental observations. Fig. 3 (left) compares steady aspect ratios obtained from experimental measurements to numerical calculations. Both datasets are in reasonable agreement, with aspect ratios between 1.4–1.6 over the range of angles explored experimentally. We interpret these aspect ratios (for $\phi > 5°$) as being roughly constant.

The existence of a steady shape (i.e. favored aspect ratio) for finite, non-zero, upper boundary angles can be inferred by assuming a balance between energy dissipation and the rate at which gravitational potential energy is lost by the bubble. Similar reasoning has been applied to different problems involving the motion of immiscible drops in viscous fluids [17]. Although viscous dissipation in the squeeze layer between the bubble and the sloping boundary can be important for immiscible fluids [15–17], here it can be neglected because of the absence of capillary effects for miscible fluids and the free-slip boundary condition ($\lambda \ll 1$) between the bubble and the lubricating film. For the sake of this argument, we assume that the aspect ratio of the bubble is mostly independent

of the slope angle ϕ as observed in both numerical calculations and experiments (Fig. 3). We thus assume that $\pi\phi/180 \ll 1$ and $b \approx a$ for the sake of the following scaling argument. The viscous dissipation associated with the bubble's motion in the (x, y) plane therefore occurs within the ambient fluid in a volume V_f proportional to the volume of the rising bubble V.

$$V_f \sim \frac{V}{\phi} \propto a^3. \quad (13)$$

Viscous dissipation scales as

$$\dot{E}_{\text{dis}} \propto \mu_1 \left(\frac{\langle u \rangle}{a} \right)^2 V_f. \quad (14)$$

The rate of gravitational potential energy loss scales as

$$\dot{E}_{\text{pot}} \propto \Delta\rho g \langle u \rangle \phi V. \quad (15)$$

The balance between these two terms leads to

$$\langle u \rangle \propto \frac{\Delta\rho g V^{2/3} \phi^{4/3}}{\mu_1}, \quad (16)$$

implying that

$$\frac{\langle u \rangle}{U} \propto \phi^{4/3}, \quad (17)$$

where U is the velocity scale defined by Eq. (16). Fig. 3 (right) compares the velocity of the bubble in the x direction obtained from experimental measurements and numerical results. The scaling relationship of Eq. (17) is shown in Fig. 3 (right) for reference. Both results exhibit the same general trend (roughly linear dependence of the velocity on the angle). However, the numerical results tend to systematically over-estimate the experimental data. As noted previously, the velocity scales with the square of the maximum thickness of the bubble. Comparing the mass distribution of the real bubble (Fig. 1) with the parametrization used in the theoretical model (Fig. 2), we observe that the maximum thickness of the bubble is over-estimated by the theoretical model, which does not include the bulge at the front of the bubble. The relative size of the bulge does not depend on ϕ within the range of angles studied experimentally, and hence, the relative discrepancy between experimental and numerical results remains a constant fraction of the bubble velocity.

Fig. 4 (left) shows the time required for the bubble to adjust to its steady shape, estimated from Eq. (12). The divergence of the time when the upper boundary becomes horizontal is reminiscent of a critical slowing down close to the critical point ($\phi = 0$) of a phase transition, where the time to reach a new equilibrium configuration diverges as a power-law as the order parameter (ϕ) approaches its critical value. The time to reach a steady bubble shape
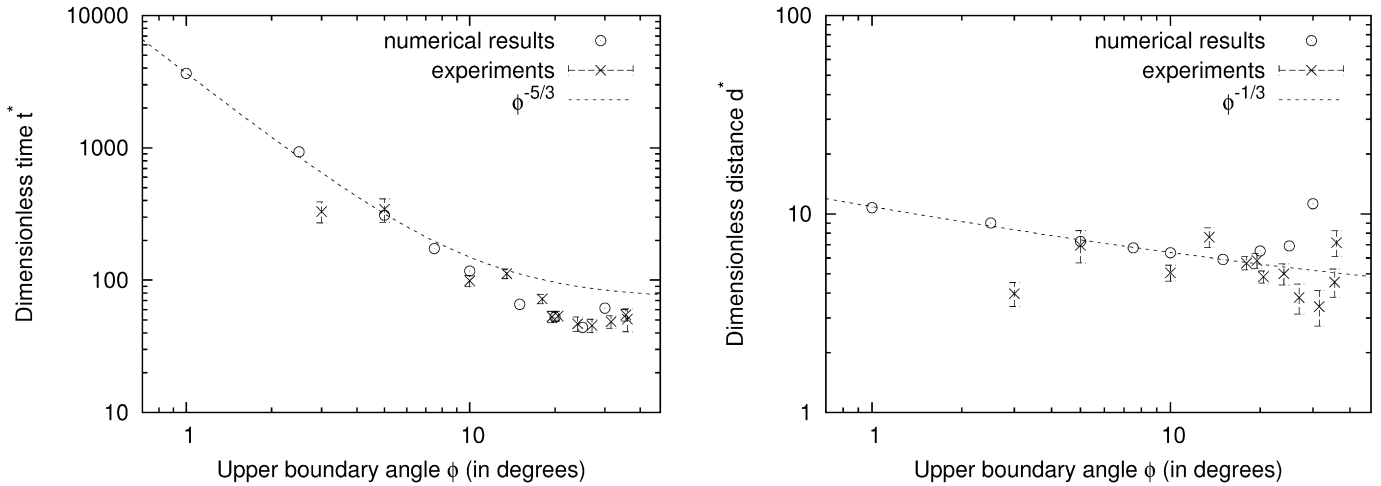
Fig. 4. (Left) Time to reach the steady aspect ratio defined by Eq. (7) normalized by R/U. The scaling relationship of equation 20 provides a first approximation to the dynamic critical exponent $\beta = -5/3$. (Right) Horizontal distance traveled before reaching the steady aspect ratio, normalized by R, the power-law dependence calculated by the scaling relationship obtained in Eq. (21), $d \propto \phi^{-1/3}$, is also represented here. The error bars for the numerical calculations are smaller than the symbols.

for small ϕ can be estimated by comparing the bubble spreading velocity along an horizontal boundary u_{sp}, which according to lubrication theory [10,14] scales as

$$u_{sp} \propto \left(\frac{\Delta \rho g V^2}{\mu} \right)^{1/5} t^{-4/5}, \tag{18}$$

to the ascent velocity of the bubble along the wall,

$$\langle u \rangle \propto \Delta \rho g (a\phi)^2 / \mu_1. \tag{19}$$

Substituting $a = (V r / \tan \phi)^{1/3}$, where r is the aspect ratio of the bubble ($\sim cst$), and solving for t, these velocities are comparable when

$$t \propto \phi^{-5/3}. \tag{20}$$

This scaling relationship is plotted on Fig. 4 (left) and is consistent with the data. The slowing down we observe should not be attributed solely to a critical phenomena in the vicinity of the phase transition, but also to the slower dynamics at small angle ϕ. It is important to note that even for very small angles, a steady bubble shape exists, although the time required for the bubble to reach the steady shape increases dramatically. Moreover, at small angles, the experimental error on the slope, and the possible bending or surface roughness of the plate, can have a large influence on the aspect ratio. At $\phi = 3°$, the width of the bubble is large enough to interact with the tank boundaries and the duration of the experiment is long enough that mass loss through diffusion can no longer be neglected (diffusion length ~ 1 mm, more than 10% of the mean thickness of the bubble). Consequently, the approach to steady-state is perturbed and the reliability of the measurements is reduced. Nevertheless, Figs. 3 and 4 clearly show that experiments and numerical results follow the same trend, even when the slope of the upper boundary is small ($\phi \sim 5°$).

Fig. 4 (right) shows the estimated horizontal distance that the bubble travels before reaching a steady aspect ratio. Unlike time, distance should not be affected by the slowing down of the dynamics at low angles. We can estimate the distance traveled by the bubble before it reaches a steady shape from the scaling relationship (20) and the projection of the bubble ascent velocity on the inclined wall (19),

$$d \sim \langle u \rangle t \propto \phi^{-1/3}. \tag{21}$$

Fig. 4 (right) shows that this power-law relationship is again consistent with our results.

6. Concluding remarks

Our study reveals the existence of a steady shape for a bubble rising beneath an inclined boundary unlike the case where the upper boundary is horizontal in which spreading is symmetric [18, 19]. The behavior of the bubble aspect ratio is reminiscent of a continuous phase transition at $\phi_{critical} = 0$ (according to the theory of [30]). Further evidence for this phase transition includes (1) a critical slowdown as the angle approaches the critical value and (2) a constant aspect ratio (1.4–1.6) for $5 < \phi < 35$. Other examples of a phase transition occurring via the breaking of symmetry are (1) ferro-magnetism [31,32] and (2) some crystal polymorphs (see for example [33]). In both of these cases, the low symmetry phase ($\phi \neq 0$) is a subgroup of the high symmetry phase ($\phi = 0$), which is characteristic of continuous phase transitions. For a horizontal upper boundary, the system has an axial symmetry about the z direction. Upon introducing a slope to the upper boundary, the symmetry is broken by the projection of the buoyancy force on the horizontal plane (x, y).

In summary, the simplified parameterization introduced in Section 4 is able to capture the essential behavior of the experiments. Our results also show that the angle of the upper boundary ($5 < \phi < 35$) has a limited effect on the steady bubble aspect ratio.

Acknowledgements

Appendix A. Green's functions

The Lorentz–Blake Green's functions for the velocity are given by

$$J^{St}_{ij}(\mathbf{x}) = \frac{\delta_{ij}}{|\mathbf{x}|} + \frac{x_i x_j}{|\mathbf{x}|^3}, \tag{22}$$

$$J^{D}_{ij}(\mathbf{x}) = \pm \left(\frac{\delta_{ij}}{|\mathbf{x}|^3} - 3 \frac{x_i x_j}{|\mathbf{x}|^5} \right), \tag{23}$$

$$J^{SD}_{ij}(\mathbf{x}) = x_1 J^{D}_{ij}(\mathbf{x}) \pm \frac{\delta_{j1} x_i - \delta_{i1} x_j}{|\mathbf{x}|^3} \tag{24}$$

where the plus sign is chosen when j is not coinciding with the direction normal to the plane of the wall. The different members of the associated stress tensor are

$$K_{ijk}(\mathbf{x}) = -6\frac{x_i x_j x_k}{|x|^5}, \tag{25}$$

$$K^D_{ijk}(\mathbf{x}) = \pm 6\left(-\frac{\delta_{ik}x_j + \delta_{ij}x_k + \delta_{kj}x_i}{|\mathbf{x}|^5} + 5\frac{x_i x_j x_k}{|\mathbf{x}|^7}\right), \tag{26}$$

$$K^{SD}_{ijk}(\mathbf{x}) = x_1 K^D_{ijk}(\mathbf{x}) \pm 6\left(\frac{\delta_{ik}x_j x_1 - \delta_{j1}x_i x_k}{|\mathbf{x}|^5}\right). \tag{27}$$

These definitions are valid for a Cartesian reference frame aligned with the boundary. The Green's function were calculated in their original reference frame and then rotated to the natural reference frame of our parametrization (x, y, z of Fig. 2) for the sake of the integrations.

References

[1] C.V. Boys, Soap Bubbles – Their Colours and the Forces which Mould Them, Dover, New York, 1959.
[2] M. Kojima, E.J. Hinch, A. Acrivos, Film flow down an inclined plane over a three-dimensional obstacle, Phys. Fluids 27 (1984) 19–32.
[3] C.J. Koh, L.G. Leal, Stability of drop shapes for translation at zero Reynolds number through a quiescent fluid, Phys. Fluids A 1 (1989) 1309–1313.
[4] C.J. Koh, L.G. Leal, An experimental investigation on the stability of viscous drops translating through a quiescent fluid, Phys. Fluids A 2 (1990) 2103–2109.
[5] C.M. Pozrikidis, The instability of a liquid drop moving normal to a plane wall, J. Fluid Mech. 215 (1990) 331–363.
[6] A.B. Subramaniam, M. Abkarian, L. Mahadevan, H.A. Stone, Non-spherical bubbles, Nature 438 (2005) 930.
[7] M. Manga, H.A. Stone, Buoyancy-driven interactions between deformable drops at low Reynolds numbers, J. Fluid Mech. 256 (1993) 647–683.
[8] M. Manga, H.A. Stone, Collective hydrodynamics of deformable drops and bubbles in dilute suspensions at low Reynolds numbers, J. Fluid Mech. 300 (1995) 231–263.
[9] J.R. Lister, R.C. Kerr, The propagation of two-dimensional and axisymmetric viscous gravity currents at a fluid interface, J. Fluid Mech. 203 (1989) 215–249.
[10] D.M. Koch, D.L. Koch, Numerical and theoretical solutions for a drop spreading below a free fluid surface, J. Fluid Mech. 287 (1995) 251–278.
[11] R.W. Griffiths, L.H. Campbell, Interaction of mantle plume heads with the earth's surface and onset of small-scale convection, J. Geophys. Res. 96 (1991) 18295–18310.
[12] D. Snyder, S. Tait, A flow-front instability in viscous gravity currents, J. Fluid Mech. 369 (1998) 1–21.
[13] H.E. Huppert, Flow and instability of a viscous current down a slope, Nature 300 (1982) 427–429.
[14] J.R. Lister, Viscous flow down an inclined plane from a point and lines sources, J. Fluid Mech. 242 (1992) 631–653.
[15] P. Aussillous, D. Quéré, Bubbles creeping in a viscous liquid along a slightly inclined plane, Europhys. Lett. 59 (2002) 370–376.
[16] K.M. DeBisschop, M.J. Miksis, D.M. Eckmann, Bubble rising in an inclined channel, Phys. Fluids 14 (2002) 93–106.
[17] S.R. Hodges, O.E. Jensen, J.M. Rallison, Sliding, slipping and rolling: the sedimentation of a viscous drop down a gently inclined plane, J. Fluid Mech. 512 (2004) 95–131.
[18] C. Kincaid, J.-G. Schilling, C. Gable, The dynamics of off-axis plume-ridge interaction in the uppermost mantle, Earth Planet. Sci. Lett. 137 (1996) 29–43.
[19] C. Kincaid, D.W. Sparks, R. Detrick, The relative importance of plate-driven and buoyancy-driven flow at mid-ocean ridges, J. Geophys. Res. 101 (1996) 16177–16193.
[20] J.B. Murphy, G.L. Oppliger, G. Brimhall, A. Hynes, Plume-modified orogeny: An example from the Western United States, Geology 26 (1998) 731–734.
[21] P.D. Ihinger, J.M. Watkins, J.E. Bernhardt, B.R. Johnson, Yellowstone plumehead meets farallon slab: a plausible mechanism driving North American continental tectonics for 80 my, in: Rocky Mountain/Cordilleran GSA, Abstracts, 36, 2004, pp. 95–96.
[22] M. Manga, H.A. Stone, R.J. O'Connell, The interaction of plume heads with compositional discontinuities in the Earth's mantle, J. Geophys. Res. 98 (1993) 19,979–19,990.
[23] G.R. Ziegler, A.L. Benado, S.S.H. Rizvi, Determination of mass diffusivity of simple sugars in water by the rotating disk method, J. Food Sci. 52 (1987) 501–502.
[24] P. Olson, H. Singer, Creeping plumes, J. Fluid Mech. 158 (1985) 511–531.
[25] C. Pozrikidis, Boundary Integral and Singularity Methods for Linearized Viscous Flow, Cambridge Texts in Applied Mathematics, 1992.
[26] M.G. Blyth, C.M. Pozrikidis, Film flow down an inclined plane over a three-dimensional obstacle, Phys. Fluids 18 (2006) 1–14.
[27] W.S. Uijttewaal, E.-J. Nijhof, R.M. Heethaar, Droplet migration, deformation, and orientation in the presence of a plane wall: A numerical study compared with analytical theories, Phys. Fluids 5 (1993) 815–825.
[28] A.J. Addlesee, K. Cornwell, Liquid film thickness above a bubble rising under an inclined plate, Trans. I. Chem. E. 75 (1997) 663–667.
[29] H.E. Huppert, The propagation of two-dimensional and axisymmetric viscous gravity currents over a rigid horizontal surface, J. Fluid Mech. 121 (1982) 43–58.
[30] L. Landau, Collected Papers of L.D. Landau, Pergamon, Oxford, 1965, 1937.
[31] A.P. Cracknell, The application of Landau's theory of continuous phase transitions to magnetic phase transitions, J. Phys. C: Sold. St. Phys. 4 (1971) 2488–2500.
[32] F. Baroni, L. Casetti, Topological conditions for discrete symmetry breaking and phase transitions, J. Phys. A: Math. Gen. 39 (2006) 529–545.
[33] J.L. Birman, Simplified theory of symmetry change in second-order phase transitions: Application to V_3Si, Phys. Rev. Lett. 17 (1966) 1216–1219.